# Direct measurement of hairpin-like vortices in the bottom boundary layer of the coastal ocean

Edward C. C. Steele,[1] W. Alex M. Nimmo-Smith,[1] and Andrey Vlasenko[2]

**Key Points.**

- The ocean bottom boundary layer comprises "packets" of hairpin-like vortices.
- Vortices occur 3.5% of the time and are aligned at ∼ 8° and inclined at ∼ 27°.
- This is directly in line with predictions based on lower Reynolds number data.

---

Corresponding author: Edward C. C. Steele, Plymouth University, Drake Circus, Plymouth, PL4 8AA, UK. (edward.steele@plymouth.ac.uk)

[1] Plymouth University, Drake Circus,
Plymouth, PL4 8AA, UK

[2] Universität Hamburg, Mittelweg 177,
20148 Hamburg, Germany

Laboratory measurements and numerical modelling at low Reynolds numbers ($Re_\theta < 7,700$) indicate the energy-containing turbulence of boundary layer flows comprises coherent packets of hairpin vortices. Here, direct measurements in the bottom boundary layer of the coastal ocean at higher Reynolds numbers ($Re_\theta = 266,150$) show tidal flows also contain packets of large vortices separated by periods of more quiescent conditions. The 1452 vortices recorded within a 20 min period are typically aligned along-stream ($\sim$8.0° from the mean flow direction) and inclined to the horizontal ($\sim$27.0° from the seabed), with a mean period of occurrence of 4.3 sec. These results lend three-dimensional, in-situ support to an interpretation of the coastal ocean bottom boundary layer as comprising coherent packets of hairpin vortices. This demonstrates a direct linkage from low Reynolds number experiments to higher Reynolds number flows, permitting fine-scale details of particle transport and pollutant dispersion to be inferred from lower Reynolds number data.

## 1. Introduction

Turbulence in shelf-seas has a strong influence on the large-scale distribution of biological production [*Tett et al.*, 1993] and suspended sediments [*Jago and Jones*, 1998]. Tidally-generated turbulence limits the areas of thermal stratification [*Simpson and Hunter*, 1974], which in turn affects the shelf-sea "pumping" of carbon dioxide and is an important process for the global carbon cycles [*Thomas et al.*, 2004]. Modelling work has also shown that small changes in the vertical distribution of the stress associated with turbulence can have a strong effect on the patterns of circulation at much larger scales [*Lentz*, 1995]. In tidal flows, turbulence is generated near the seabed [*Heathershaw*, 1974]. However, while its one-dimensional characteristics have been well-studied [*Burchard et al.*, 2008], little is known of its three-dimesional structure and subsequent development throughout the water column. On reaching the surface of well-mixed waters, bottom-generated "boils" – areas of local upwelling and associated eddies – have a marked impact on the dispersion of pollution and the contributes to the replacement of surface waters from depth [*Nimmo-Smith et al.*, 1999; *Thorpe et al.*, 2008].

Laboratory measurements [*Adrian et al.*, 2000a; *Ganapathisubramani et al.*, 2006; *Dennis and Nickels*, 2011] and numerical modelling [*Zhou et al.*, 1999; *Adrian and Liu*, 2002; *Wu and Moin*, 2009] indicate the energy-containing turbulence of boundary layer flows comprises coherent packets of "hairpin" vortices [*Robinson*, 1991]. These have a specific – but rarely, if ever, perfectly symmetrical – form that, in an ideal case, consists of a cross-stream arch (made up of both head and neck components) with two counter-rotating along-stream legs (Figure 1A). The induction of the flow surrounding the eddy causes an upward "burst" between the head and legs. It is here that vorticity elements are focused (i.e. stronger over a small area of influence) and, in turn, cause an area of low-momentum fluid below and upstream of the arch. Outside the area between the head and legs, fluid flows down and forward, forming a "sweep". The induction of the flow here is unfocused (i.e. weaker over a large area of influence) and so the strength of the burst exceeds that of the sweep. The opposing burst / sweep motion causes a shear layer, inclined at 25-45° from the boundary [*Adrian*, 2007]. Two-dimensional flow visualisation methods have previously shown that these coherent structures (i.e. elementary organised motions that exhibit both spatial and temporal persistence) also exist in the bottom boundary layer of tidal flows (Figure 1B) [*Nimmo-Smith et al.*, 2002, 2005; *Hackett et al.*, 2011]. Conditional sampling based on vorticity revealed that these coherent structures contribute most to the Reynolds stress and, as such, are the key areas where energy is extracted from the mean flow and into turbulence [*Nimmo-Smith et al.*, 2005]. However, questions remain as to the full three-dimensional form of such coherent structures, that may eventually grow into the depth-scale boils seen at the sea surface [*Adrian and Marusic*, 2012].

Here, for the first time, we present an analysis of the instantaneous three-dimensional form of turbulence in the bottom boundary layer of a tidal flow. The measurements shed light on the dynamical phenomena responsible for the statistical properties that are traditionally recorded by standard instrumentation or obtained through numerical modelling, providing in-situ evidence to support an interpretation of the bottom boundary layer of the coastal ocean as comprising coherent structures consistent with laboratory and numerical experiments presented in the scientific literature.

## 2. Methods

### 2.1. Instrumentation

The measurements were made using a submersible three-dimensional Particle Tracking Velocimetry (3D-PTV) system [*Nimmo-Smith*, 2008]. 3D-PTV is a robust method for the visualisation of flow structures [*Adrian*, 1991], and has been used in the laboratory to study the boundary layer of free-surface flow [*Virant and Dracos*, 1997] and the properties of isotropic turbulence [*Ott and Mann*, 2000; *Lüthi et al.*, 2005]. The method uses multiple synchronous cameras to view a sample volume from different angles, in which small neutrally-buoyant suspended particles are located and tracked in three dimensions, allowing the full velocity field to be determined. Due to the impracticality of seeding particles within the flow, naturally-occurring suspended particles are used as tracers. Briefly, the 3D-PTV system uses four high-resolution digital cameras ($1004 \times 1004$ pixels, 8 bit) to view a $20 \times 20 \times 20\,\mathrm{cm}^3$ sample volume that is illuminated by four 500 W underwater lights. Images from the cameras are recorded at a rate of 25 Hz directly to hard disk storage. The cameras, lights and data acquisition system, all within underwater housings, are mounted on a rigid frame. A vane attached to the frame aligns it at an angle to the mean flow to prevent contamination of the sample volume by the wake of the system. A acoustic Döppler current profiler (1200 kHz ADCP) and an acoustic Döppler velocimeter (ADV) monitors this alignment, also providing turbulence statistics at the same height as the sample volume. A second, vessel-mounted, acoustic Döppler current profiler (600 kHz ADCP) was also used to obtain the background flow conditions.

### 2.2. Data processing

Calibration of the system is conducted in situ, just prior to sampling, using a moving single-point target and a self-calibration process [*Svoboda et al.*, 2005]. The calibration accounts for both the outer-positioning and the alignment of the cameras, as well as any distortion within the imaging systems.

Data processing is completed in three stages using specialist "Particle Tracking Velocimetry" software [*Maas et al.*, 1993; *Willneff*, 2003]. Firstly, particles are located in the raw camera images using a high-pass filter, threshold segmentation and weighted centroid methods. Size thresholds are also used to minimise contamination from noise or large-objects. Secondly, three-dimensional correspondence between particle images from each camera are made for each set of synchronised images, using the calibration information to give instantaneous three-dimensional distributions of particle locations. Thirdly, tracking of the particles is performed in both image and object space, running the sequence in both directions to maximise possible linkages between adjacent frames. The spatio-temporal tracking algorithm used improves tracking efficiency, allowing higher particle densities and providing longer particle trajectories even in complex turbulent flows. Under optimal conditions the 3D-PTV system can track more than 1,000 particles simultaneously. Naturally-occurring suspended particles (plankton and sediment flocs) are used as tracers as they are carried by the combined mean flow, orbital wave motion and turbulence. These particles are located in the sample volume to within 0.25 mm, limited by the irregularity of the particles and the resolution of the cameras. At each time-step, the velocity of every particle is calculated by low-pass filtering its position information using a moving cubic spline [*Lüthi et al.*, 2005]. To account for the increase in noise level associated with tracking unevenly-shaped naturally occurring tracers scattered inhomogeneously within the sample volume, the velocity data are projected onto a regular grid where its adherence to the governing hydrodynamical principles of fluid flows is enforced by the Vorticity Transport Equation, using a Physics-Enabled Flow Restoration Algorithm [*Vlasenko et al.*, 2015].

### 2.3. Vortex identification

A vortex can be identified using the characteristic roots of the velocity gradient tensor, $\nabla \mathbf{u}$ [*Chong et al.*, 1990; *Dallman et al.*, 1991] and the streamlines containing the core said to be spiralling where two of these roots form a complex-conjugate pair [*Zhou et al.*, 1999]. The swirling strength of this core (i.e. the magnitude of the imaginary part of these complex roots, $\lambda_{ci}$) is both quantitatively and qualitatively similar to the vorticity, however it is only associated with the asymmetric part of $\nabla \mathbf{u}$ corresponding to rotation and discriminates against the symmetric part of $\nabla \mathbf{u}$ corresponding to shear. It is frame-independent, with a firm mathematical basis and unambiguous physical interpretation [*Adrian et al.*, 2000b; *Chakraborty et al.*, 2005].

Vortices are extracted by $\lambda_{ci} > N$, where $N$ is an arbitrary threshold; typically a few percent of the data maximum, as deduced by an examination of the velocity, vorticity and swirling strength distributions. While theoretically setting $N = 0$ is sufficient to enable vortex identification, a higher threshold of $\lambda_{ci}$ yields a smoother output, facilitating visualisation. *Zhou et al.* [1999] established that the general topology of a vortex is independent of the magnitude of the $\lambda_{ci}$ threshold used, with characteristics such as the tilt angle of the vortex heads / legs, the along-stream distance between successive vortex heads and the cross-stream distance between the vortex legs all remaining unaffected. However, as the diameter and the length of the vortex changes with the specific magnitude of the $\lambda_{ci}$ threshold used, these properties are not generally reported.

To limit the effect of noise, a $3 \times 3 \times 3$ box filter is applied to the data and a $\lambda_{ci} = 0.25\,\mathrm{s}^{-1}$ threshold is used. This is consistent with the approach employed in existing in-situ two-dimensional flow visualisation measurements by *Hackett et al.* [2011]. To prevent erroneous inferences based on vortices consisting of only a few points, only the statistics from those occupying at least 1.0% of the sample volume are counted.

### 2.4. Deplyments and data

The 3D-PTV system was deployed on the east side of Plymouth Sound, Plymouth, UK in about 12 m deep water. Here, the seabed is flat and consists of firm sand and mud, without notable ripples or other bed forms. During the period when data were collected, mean near-surface currents reached $0.22\,\mathrm{m\,s}^{-1}$, however the site was sheltered from most surface wave motion by an artificial breakwater. Although in a region of freshwater input, the water column was vertically well-mixed with no density stratification. Following deployment and calibration, the system was lowered close to the seabed and allowed to orientate at an angle to the mean flow direction before being set down. Data were sampled in ten 20 min duration segments spaced over 5 hours of an ebb tide, with the centre of the sample volume in the logarithmic part of the boundary layer velocity profile at a height of 0.64 m ($z^+ = 1.7225 \times 10^3$ non-dimensional wall units) above the seabed. The Reynolds number of the flow, based on the momentum thickness, determined by integration of the time-averaged velocity profile recorded by the ADCPs [*Pope*, 2000], is $Re_\theta = 266,150$. The details of this calculation, and the plot of the time-averaged velocity profile recorded by the ADCPs, is provided as *supporting information*. The data reported here are from one of the segments recorded about 2 hours after high water, during the acceleration phase of the tide. On average, 150 particles are tracked over each time-step usually giving more than 100 instantaneous velocity vectors.

## 3. Results and discussion

Figure 2A presents a time series of the sample volume mean turbulence intensity over the 20 min period, revealing the patchiness within the flow characterised by both small and large peaks. All the peaks correspond to patches of enhanced turbulence. The small peaks can be attributed to minor fluctuations within the flow or turbulence scales too small for the instrument to resolve clearly [*Nimmo-Smith*, 2008; *Vlasenko et al.*, 2015], while the large peaks can be attributed to simple regions of vertical shear or the passage of large coherent vortices. Importantly, these large peaks do not occur randomly, nor exist in isolation, but exhibit the temporal persistence typical of the passage of a packet of hairpin vortices through the sample volume [*Adrian*, 2007]. This is highlighted in Figure 2B for a 10 sec subset of the data where a section of high turbulence intensity is seen to be surrounded by sections of low turbulence intensity. In each plot, each of the individual velocity flow fields where a vortex was detected are marked, comprising a total of 1452 vortex components (in 1426 instantaneous realisations of the sample volume) over the 20 min period (i.e. 29,991 instantaneous realisations of the sample volume). To account for the same eddies being tracked over multiple frames, an uninterrupted sequence of vortices (recorded in successive frames) is treated as a single eddy and used to compute a mean period between vortices of 4.3 sec.

The interpretation of this is that for most (96.5 %) of the time, the flow is quiescent, with little apparent structure, or with scales that are too small for the instrument to resolve clearly. Figure 2C presents an example velocity flow field where the sample volume mean velocity has been subtracted from each individual velocity vector to reveal the weak motion of the turbulence. Here, the flow is mostly laminar but small (diameter $< 5$ cm) vortices, such as seen on the left hand side of the volume, may also occur. In contrast to the moderately quiescent conditions are the example eddies presented in Figure 2D and Figure 2E. These large vortices with a diameter of 5-15 cm occur intermittently either singly or in groups and remain coherent for at least the time that they are advected through the sample volume by the mean flow ($\sim$2 sec). Of the many of different orientations present, some vortices exhibit cores aligned approximately cross-stream (Figure 2D), or "arced" cores comprising an along-stream section in their lower parts, that are similar to the head and neck component of hairpin vortices, respectively. Additionally, others are aligned as along-stream legs (Figure 2E), usually inclined from the seabed. It is clear, however, that this visualisation is limited by the size of the 3D-PTV sample volume, meaning that an extended volume of flow is needed to be able to see the eddies in context.

The larger scales of the turbulence can be revealed using a frozen-field approximation (Taylor's Hypothesis) and offsetting the data within the instantaneous realisations of the sample volume according to the sampling rate and the instantaneous mean velocity. Taylor's Hypothesis ($x_i = U_i t$) allows the spatial projection of temporal data, assuming the characteristics of the eddies remain unchanged with advection past the sensor and $\langle u^2\rangle/\langle U^2\rangle \ll 1$ where, here, $\langle u^2\rangle/\langle U^2\rangle = 0.04$ is the ratio of the mean-square of the zero-mean velocity to that of the mean velocity and angle brackets denote an ensemble average [*Taylor*, 1938]. *Dennis and Nickels* [2008] established that this method is accurate over a projection distance of more than $6\delta$ where, here, $\delta = 9.45\,\mathrm{m}$ is the boundary layer thickness. The details of this calculation, and the plot of the time-averaged velocity profile recorded by the ADCP, is provided as *supporting information.*

As an example, the results of applying this method to the 10 sec interval around the structure presented in Figure 2D, giving a volume of flow measuring $190 \times 20 \times 20\,\mathrm{cm}^3$, are presented in Figure 3A. Rotating around the volume in three-dimensions (as is possible in Movies M1 to M3 provided as supporting information), the large cross-stream vortex is readily visible (II), with a second large inclined along-stream vortex (III) seen upstream and lower down than the first. The first vortex appears to be curling around from along-stream to cross-stream with distance downstream. The two vortices appear intertwined and together have an along-stream length in excess of 50 cm. This coherent structure is surrounded by more quiescent flow conditions (I and IV), although these again contain evidence of small scale vortical motion.

The vorticity characteristics of the extended volume are presented in Figure 3B. This is the three-dimensional equivalent of the planar evidence provided by *Nimmo-Smith et al.* [2002, 2005] and *Hackett et al.* [2011] that have shown the counter-clockwise and clockwise rotation of cross-stream vortices within the bottom boundary layer of the coastal ocean.

The large cross-stream vortex (labelled "vortex") exhibits clockwise rotation (negative vorticity) consistent with a "head".

To complement the visualisation of the velocity and vorticity characteristics of these flows, the spatial measurements recorded by the 3D-PTV are used to determine $\lambda_{ci}$ of the fluid. Figure 3C presents the three-dimensional iso-surface of $\lambda_{ci}$, as well as the iso-surface of the negative and positive zero-mean along-stream velocity ($u = \pm 1$ cm s$^{-1}$). The agreement between the loci of the vortices and the negative along-stream velocity are completely consistent with the pattern of the velocity flow field expected of a packet of hairpin vortices. These vortices (white iso-surfaces, e.g. large cross-stream vortex labelled 'II') straddle sections of negative zero-mean along-stream velocity (blue iso-surface), the part of the flow between the head and legs, while the part of the flow outside the area between the head and legs has a positive zero-mean along-stream velocity (red iso-surface). Examination of the 3D-PTV data suggests that, like here, vortices often appear to be asymmetric, i.e. having one leg stronger than the other, giving an appearance similar to a"walking-cane". This cane-like topology is, in fact, the most probable condition [*Robinson*, 1991], since individual eddies are affected by other large scale motions within the velocity flow field. Similar results have been presented in data collected by *Dennis and Nickels* [2011], with an "ideal" hairpin only revealed through conditional sampling.

Statistical evidence of hairpin vortices (or, more accurately, "hairpin-like" vortices - a term encompassing canes, heads, necks, legs and three-quarter-hairpin vortices) in-situ is yielded from an assessment of their orientation from the mean flow direction and the seabed, respectively. To establish the link with laboratory measurements and numerical modelling, it is apparent (on average) one vortex must be aligned as a cross-stream head for every two aligned as along-stream legs, and these are inclined from the seabed at an angle of 25-45 ° [*Adrian*, 2007]. To compute the along-stream/cross-stream orientation from the mean flow direction ($\alpha_{xy}$) and the along-stream/wall-normal orientation from the seabed ($\alpha_{xz}$), all connected points within the iso-surface of $\lambda_{ci} > 0.25\,\mathrm{s}^{-1}$ are identified. A three-dimensional least-squares line (1st order polynomial) is fitted to each set of connected points and the minimum and maximum along-stream coordinates are used to compute $\alpha_{xy}$ and $\alpha_{xz}$ trigonometrically. Note that data are from an analysis of each set of points from each of the instantaneous realisations of the sample volume to account for the multiple component angles within the vortex (e.g. its head, neck and legs) and, therefore, the compiled statistics represent an aggregation of these different parts. This is conducted using the 20 min time-series, rather than being based on data from an extended volume, to ensure that statistics are representative. Figure 4A presents a histogram of the along-stream/cross-stream orientation of vortices, binned according to their angle ($\alpha_{xy}$) from the mean flow. The ratio of cross-stream components ($|\alpha_{xy}| > 45$) to along-stream components ($|\alpha_{xy}| < 45$) is 596:856, with a most common along-stream/cross-stream orientation of $\alpha_{xy} = 8.0\,°$. Figure 4B presents a histogram of the along-stream/wall-normal orientation of vortices, binned according to their angle ($\alpha_{xz}$) from the seabed. Most of the vortices (72.4 %) are inclined at positive angles, with a most common along-stream/wall-normal angle of $\alpha_{xz} = 27.0\,°$. Setting a higher threshold of $\lambda_{ci}$ or of the minimum percentage coverage suggests that stronger vortices are inclined slightly more steeply. The shapes of the two histograms, as well as the $\alpha_{xy}$ and the $\alpha_{xz}$ angles obtained are consistent with laboratory measurements. Like here, in data presented by *Ganapathisubramani et al.* [2006] from a wind tunnel at $Re_\theta = 2,800$ and *Dennis and Nickels* [2011] from a water tunnel at $Re_\theta = 4,700$, vortices are seen to be typically aligned in an along-stream direction with a most common inclination angle of $\alpha_{xz} = 38.0\,^\circ$ and $\alpha_{xz} = 26.5\,^\circ$, respectively. These angles fall within the nominal range of 25-45 ° expected of a packet of hairpin vortices, with the exact differences between the two associated with differences in the experimental set-up and the specific way the along-stream/wall-normal angles are computed. Similarly, these vortices are predominantly inclined at positive angles from the wall (87.5 %, in data presented by *Dennis and Nickels* [2011]), supporting the idea of these boundary layer flows being made up of forward leaning cores.

These results offer the first three-dimensional evidence of hairpin-like vortices in the bottom boundary layer of the coastal ocean. From both the qualitative and quantitative analysis of the characteristics of these vortices recorded in-situ, it is clear that data collected through both laboratory and numerical experiments presented in the scientific literature are directly applicable to geophysical scales. Furthermore, the finding by *Nimmo-Smith et al.* [2005], that 'gusts' (or packets) of coherent structures contribute most to the Reynolds stress are supported by a separate analysis [*Steele*, 2015] of the covariance of $u$, $v$ and $w$ terms for the velocity flow fields presented here.

Coherent structures have been identified as important to the resuspension of sediment [*Jackson*, 1976; *Cellino and Lemmin*, 2004]) and the vortices presented here may act as a transport and trapping mechanism for non-neutrally buoyant material, e.g. oil [*Stommel*, 1949]. The cores of the vortices appear helical (e.g. Figure 2D), that may lead to the separation of different-size suspended particles, with smaller particles retained within and transported along the inner cores. It is suggested that this will affect the characteristics of aggregates near the seabed, since a settling floc trapped within a vortex may experience a higher number of collisions with other particles and therefore grow in size – at least up until the point it is sheared across the edge of the vortex.

The Reynolds numbers based on the momentum thickness (and estimated from the ADCPs) are of the order of $Re_\theta = 266,150$ (over two orders of magnitude higher than reported by *Ganapathisubramani et al.* [2006] and *Dennis and Nickels* [2011] in the laboratory). Furthermore, the moderate levels of turbulence presented here are typical of other flat, coastal sites, under calm conditions, that may be encountered over large areas of the continental shelf. However, further measurements are necessary to extend our understanding of the three-dimensional turbulence characteristics of tidal flows to more extreme conditions of larger currents and oscillatory flow over bed forms. The submersible 3D-PTV system offers a viable method to achieve this, although upgrading the hardware to use high-speed cameras will be necessary to allow faster flow-rates to be sampled. Similarly, it is anticipated that adapting the setup to allow mid-water column measurements will complement the present study by eliciting the three-dimensional turbulence characteristics associated with stratified conditions.

## 4. Conclusions

3D-PTV measurements have been performed in the bottom boundary layer of the coastal ocean at high Reynolds number. The results show that coherent structures, consistent with the hairpin-like vortices in laboratory measurements and numerical modelling, were frequently present within the logarithmic layer at a height of 0.64 m ($z^+ = 1.7225 \times 10^3$) above the seabed. These exhibit a modal along-stream/cross-stream orientation of $\alpha_{xz} = 8.0\,^\circ$ and a modal along-stream/wall-normal orientation of $\alpha_{xz} = 27.0\,^\circ$, with a mean period of occurrence of 4.3 sec, and appear to straddle sections of negative zero-mean along-stream velocity, consistent with an interpretation as "packets". From these direct measurements, it is clear that data collected through both laboratory and numerical experiments are directly applicable to geophysical scales – a finding that will enable the fine-scale details of particle transport and pollutant dispersion to be studied in future.

**Acknowledgments.** E C C Steele was funded by the School of Marine Science and Engineering, Plymouth University, Plymouth, UK. Development of the 3D-PTV system was funded by the Royal Society, the Nuffield Foundation and the UK Natural Environment Research Council, while development of the data processing method was adapted under a visiting fellowship award from the Marine Institute (Plymouth University), Plymouth, UK. The 3D-PTV data are available upon request from the authors. We are grateful to C Bunney, E Davies and D Uren for assistence with the deployment of the 3D-PTV system, and D Conley and J H Simpson for help in improving the manuscript.

## References

Adrian, R. J. (1991), Particle-imaging techniques for experimental fluid mechanics, *Annual Review of Fluid Mechanics*, *23*, 261–304.

Adrian, R. J. (2007), Hairpin vortex organisation in wall turbulence, *Physics of Fluids*, *19*, 041,301.

Adrian, R. J., and Z.-C. Liu (2002), Observation of vortex packets in direct numerical simulation of fully turbulent channel flow, *Journal of Visualisation*, *5*, 9–19.

Adrian, R. J., and I. Marusic (2012), Coherent structures in flow over hydraulic engineering surfaces, *Journal of Hydraulic Research*, *50*, 451–464.

Adrian, R. J., C. D. Meinhart, and C. Tomkins (2000a), Vortex organisation in the outer region of the turbulent boundary layer, *Journal of Fluid Mechanics*.

Adrian, R. J., K. T. Christensen, and Z.-C. Liu (2000b), Analysis and interpretation of instantaneous turbulent velcocity fields, *Experiments in Fluids*, *29*, 275–290.

Burchard, H., P. D. Craig, J. R. Gemmrich, H. van Haren, P.-P. Mathieu, H. E. M. Meier, W. A. M. Nimmo-Smith, H. Prandke, T. P. Rippeth, E. D. Skyllingstad, W. D. Smyth, D. J. S. Welsh, and H. W. Wijesekera (2008), Observational and numerical modeling methods for quantifying coastal and ocean turbulence and mixing, *Progress in Oceanography*, *76*, 399–442.

Cellino, M., and U. Lemmin (2004), In flows of coherent flow structures on the dynnamics of suspended sediment transport in open-channel flow, *Journal of Hydraulic Engineering*, *130*, 1077–1088.

Chakraborty, P., S. Balachandar, and R. J. Adrian (2005), On the relationships between local vortex identification schemes, *Journal of Fluid Mechanics*, *535*, 189–214.

Chong, M. S., A. E. Perry, and B. J. Cantwell (1990), A general classification of three-dimensional flow fields, *Physics of Fluids*, *2*, 765–777.

Dallman, U., A. Hilgenstock, B. Schulte-Werning, and H. Vollmers (1991), On the footprints of three-dimensional separated vortex flows around blunt bodies, *Proceedings of the AGARD Conference.*

Dennis, D. J., and T. B. Nickels (2008), On the limitations of Taylor's hypothesis in constructing long structures in a turbulent boundary layer, *Journal of Fluid Mechanics*, *614*, 197–206.

Dennis, D. J., and T. B. Nickels (2011), Experimental measurement of large-scale three-dimensional structures in a turbulent boundary layer; part 1: vortex packets, *Journal of Fluid Mechanics*, *673*, 180–217.

Ganapathisubramani, B., E. K. Longmire, and I. Marusic (2006), Experimental investigation of vortex properties in a turbulent boundary layer, *Physics of Fluids*, *18*(055105).

Hackett, E., L. Luznik, A. R. Nayak, J. Katz, and T. R. Osborn (2011), Field measurements of turbulence at an unstable interface between current and wave bottom boundary layers, *Journal of Geophysical Research*, *116*(C02022).

Heathershaw, A. D. (1974), Bursting phenomena in the sea, *Nature*, *248*, 394–395.

Jackson, R. G. (1976), Sedimentological and fluid-dynamic implications of the turbulent bursting phenomenon in geophysical flows, *Journal of Fluid Mechanics*, *77*, 531–560.

Jago, C. F., and S. E. Jones (1998), Observation and modelling of the dynamics of benthic fluff resuspended from a sandy beach in the southern north sea, *Continental Shelf Research*, *18*, 1255–1283.

Lentz, S. (1995), Sensitivity of the inner-shelf circulation to the form of the eddy viscosity profile, *Journal of Physical Oceanography*, *25*, 19–28.

Lüthi, B., A. Tsinober, and W. Kinzelbach (2005), Lagrangian measurement of vorticity dynamics in turbulent flow, *Journal of Fluid Mechanics*, *528*, 87–118.

Maas, H. G., A. Grun, and D. Papantoniou (1993), Particle tracking in three dimensional turbulent flows. part 1: Photogrammetric determination of particle coordinates, *Experiments in Fluids*, *15*, 133–146.

Nimmo-Smith, W. A. M. (2008), A submersible three-dimensional particle tracking velocimetry system for flow visualization in the coastal ocean, *Limnology and Oceanography: Methods*, *6*, 96–104.

Nimmo-Smith, W. A. M., S. A. Thorpe, and A. Graham (1999), Surface effects of bottom-generated turbulence in a shallow tidal sea, *Nature*, *400*, 251–254.

Nimmo-Smith, W. A. M., P. Atsavapranee, J. Katz, and T. R. Osborn (2002), PIV measurements in the bottom boundary layer of the coastal ocean, *Experiments in Fluids*, *33*, 962–971.

Nimmo-Smith, W. A. M., J. Katz, and T. R. Osborn (2005), On the structure of turbulence in the bottom boundary layer of the coastal ocean, *Journal of Physical Oceanography*, *35*, 72–93.

Ott, S., and J. Mann (2000), An experimental investigation of the relative diffusion of particle pairs in three-dimensional turbulent flow, *Journal of Fluid Mechanics*, *422*, 207–233.

Pope, S. B. (2000), *Turbulent flows*, Cambridge University Press, Cambridge, Massachusetts.

Robinson, S. K. (1991), Coherent motions in the turbulent boudnary layer, *Annual Review of Fluid Mechanics*, *23*, 601–639.

Simpson, J. H., and J. Hunter (1974), Fronts in the Irish Sea, *Nature*, *250*, 404–406.

Steele, E. C. C. (2015), Three-dimensional turbulence characteristics of the bottom boundary layer of the coastal ocean, Ph.D. thesis, University of Plymouth.

Stommel, H. (1949), Trajectories of small bodies sinking slowly through convection cells, *Journal of Marine Research*, *8*, 24–29.

Svoboda, T., D. Martinec, and T. Pajdla (2005), A convenient multi-camera self-calibration for virtual environments, *PRESENCE: teleoperators and virtual environments*, *14*, 407–422.

Taylor, G. I. (1938), The spectrum of turbulence, *Proceedings of the Royal Society of London, Series A*, *164*, 476–490.

Tett, P. B., I. R. Joint, D. A. Purdie, . Baars, S. Oosterhuis, G. Daneri, F. Hannah, D. K. Mills, D. Plummer, A. J. Pomroy, A. W. Walne, H. J. Witte, M. J. Howarth, and R. Lankeste (1993), Biological consequences of tidal stirring gradients in the north sea, *Philosophical Transactions of the Royal Society of London, Series A*, *343*, 493–508.

Thomas, H., Y. Bozec, K. Elkalay, and H. J. W. de Baar (2004), Enhanced open ocean storage of C02 from shelf sea pumping, *Science*, *304*, 1005–1008.

Thorpe, S. A., J. A. M. Green, J. H. Simpson, T. R. Osborn, and W. A. M. Nimmo-Smith (2008), Boils and turbulence in a weakly stratified shallow tidal sea, *Journal of Physical Oceanography*, *38*, 1711–1730.

Virant, M., and T. Dracos (1997), 3d-ptv and its application on lagrangian motion, *Measurement Science and Technology*, *8*, 1539.

Vlasenko, A., E. C. C. Steele, and W. A. M. Nimmo-Smith (2015), A physics-enabled flow restoration algorithm for sparse PIV and PTV measurements, *Measurement Science and Technology*, *26*, 065,301.

Willneff, J. (2003), A spatio-temporal matching algorithm for 3d particle tracking velocimetry, Ph.D. thesis, ETH Zurich.

Wu, X., and P. Moin (2009), Direct numerical simulation of turbulence in a nominally zero-pressure-gradient flat-plate boundary layer, *Journal of Fluid Mechanics*, *630*, 5–41.

Zhou, J., R. J. Adrian, S. Balachandar, and T. M. Kendall (1999), Mechanisms for generating coherent packets of hairpin vortices in channel flow, *Journal of Fluid Mechanics*, *387*, 353–396.

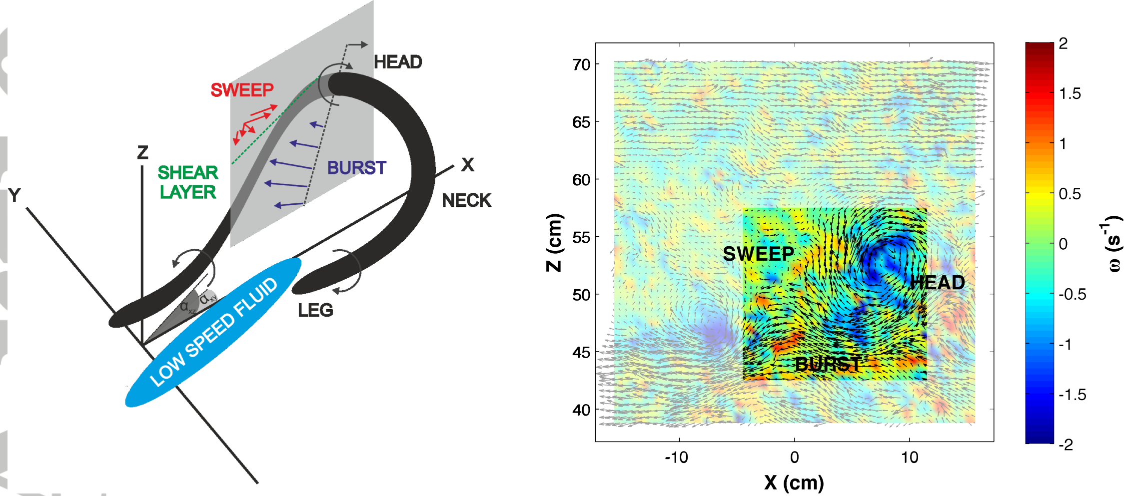

**Figure 1.** (A) Sketch of the form of a hairpin vortex in a boundary layer at a moderate Reynolds number (after Adrian, 2007). (B) Sample instantaneous zero-mean velocity and vorticity distribution corresponding to the grey plane in panel (A), obtained from 2D in-situ flow visualisation measurements in the bottom boundary layer of the coastal ocean (after *Nimmo-Smith et al.* [2005]). Angles $\alpha_{xy}$ and $\alpha_{xz}$ are the orientation of the vortex in an along-stream/cross-stream plane and an along-stream/wall-normal plane, respectivly, computed using the coordinates of the maximum and minimum along-stream extent of the isosurface containing the vortex. An identical figure, but in units of swirling strength ($\lambda_{ci}$) rather than vorticity ($\omega$) is provided as *supporting information.*

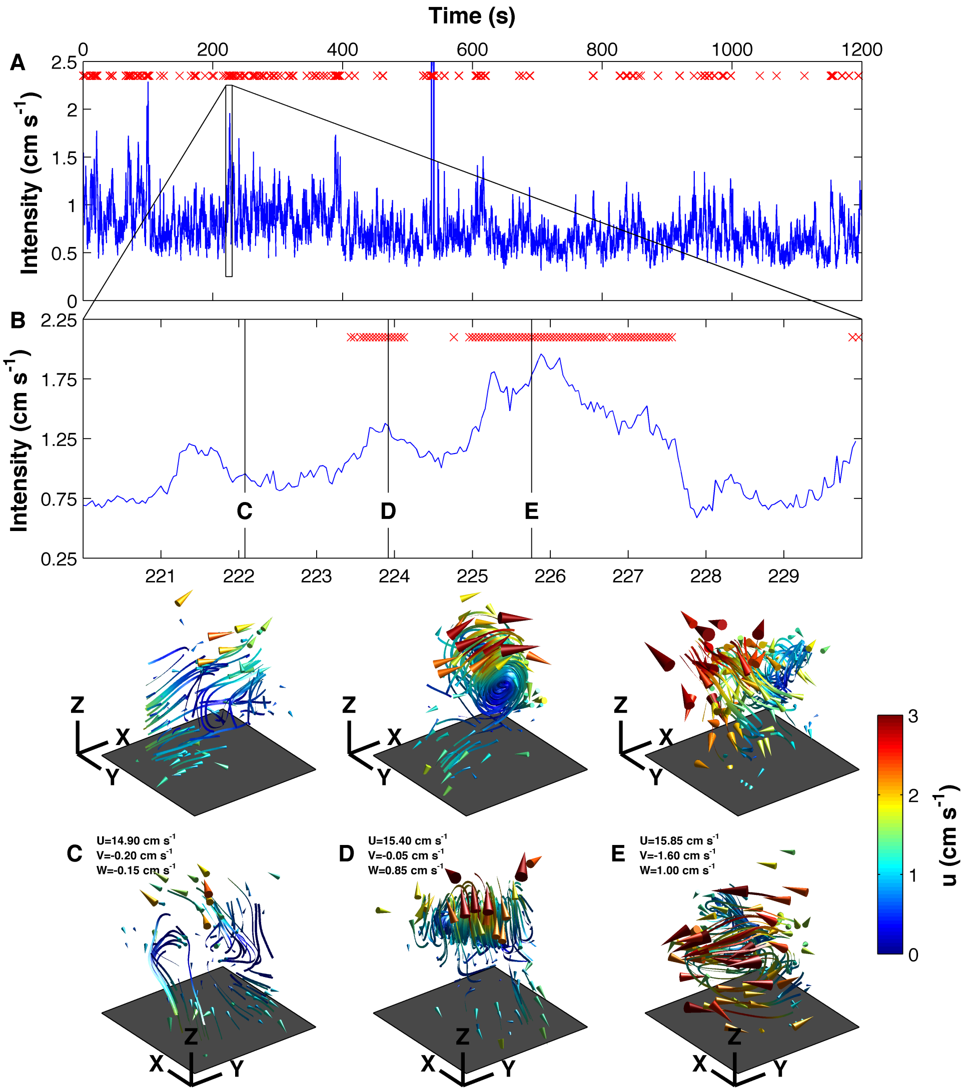

**Figure 2.** (A) Time-series of the sample volume mean turbulence intensity over a 20 min sampling period. The magnified area (B) shows the temporal persistence associated with the passage of coherent structures (marked by red crosses). (C-E) Pairs of simultaneous, instantaneous views of sample coherent structures. To reveal the turbulence structures, the sample volume mean velocity components (U, V and W) have been subtracted from each individual vector. Streamlines, starting at the position of each vector and coloured by the local velocity, illustrate the pattern of the flow. The axes are 5 cm in length, with the x-axis aligned with the mean flow.

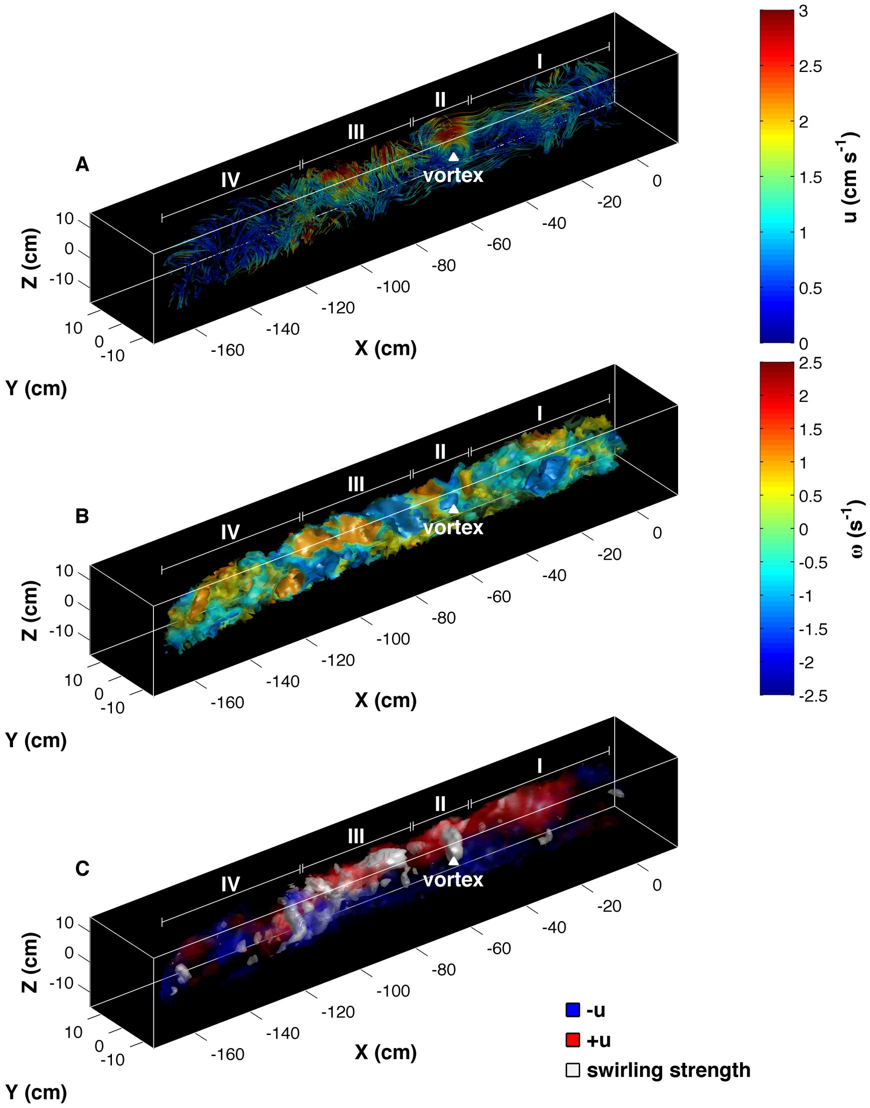

**Figure 3.** Visualisation of coherent structures within an extended volume created using a frozen field approximation. The (A) velocity; (B) vorticity ($\omega$); and (C) swirling strength ($\lambda_{ci} \geq 0.25\, s^{-1}$) used for vortex identification. Coherent structures consistent with the head, neck and legs of hairpin vortices occur within sections labelled II and III, surrounded by more quiescent flow (sections labelled I and IV). Movies, rotating around the extended volume, enabling the exploration of these inherently three-dimensional data, are provided as *supporting information*.

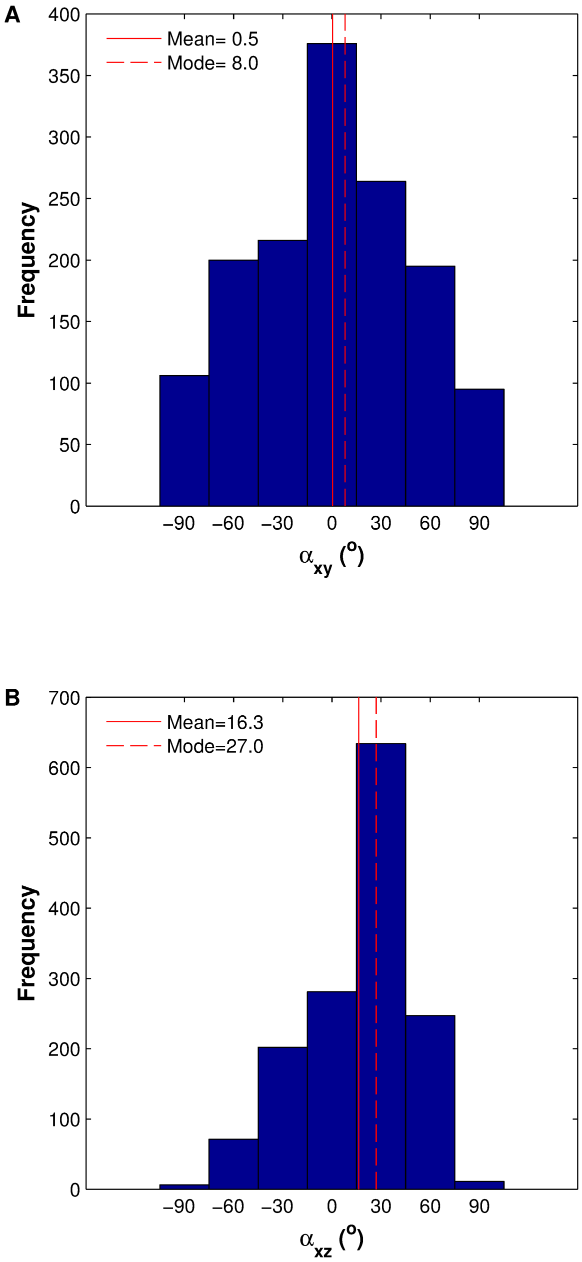

**Figure 4.** (A) Along-stream/cross-stream orientation of vortices relative to the mean flow direction (mean: 0.5 °, mode: 8.0 °, standard deviation: 47.8°). (B) Along-stream/wall-normal orientation of vortices relative to the seabed (mean: 16.3 °, mode: 27.0 °, standard deviation: 32.6°). Sample size = 1452 vortex components (recorded in 1426 instantaneous velocity flow fields).